Microwave Holographic Imaging of Non-Metallic Concentric Pipes

Hailun Wu, *Member, IEEE,* Maryam Ravan, *Senior Member, IEEE*, Raveena Sharma, Jay Patel, and Reza K. Amineh, *Senior Member, IEEE*

***Abstract*—Recently, non-metallic materials which are resilient to corrosion, low cost, and light weight, have been exploited in many industrial sectors such as oil and gas field. A common application of them is in the form of pipes. Despite the advantages, these pipes can be damaged by delamination, defects, holes, and erosion, which may lead to major production failures or even environmental catastrophes. To prevent these issues, non-destructive testing (NDT) of these pipes is required to replace these components in a timely manner. Due to the fact that the traditional NDT methods are mostly effective for metallic pipes, microwave holographic imaging is proposed for inspection of multiple concentric non-metallic pipes. Besides, standardized minimum norm (SMN) is employed to mitigate the depth biasing problem in the proposed imaging technique. In order to reduce the complexity of the imaging system, we aim at using the narrowest possible frequency band by using an array of receiver antennas. The performance of the proposed NDT method is validated through simulation and experimental data in two scenarios including the antennas placed outside the pipes and inside the pipes.**

***Index Terms*—Microwave imaging, Millimeter wave imaging, Non-destructive testing (NDT), Non-metallic pipes, Standardized minimum norm (SMN).**

I. Introduction

NON-METALLIC and composite materials such as fiber reinforced plastic (FRP), glass reinforced epoxy resin (GRE), high density polyethylene (HDPE), reinforced rubber expansion joints (REJs), carbon fiber reinforced plastics (CFRP), and polyvinyl chloride (PVC) are rapidly replacing metallic components in various industrial sectors. This is mainly due to the significant advantages such as their resilience to corrosion, light weight, and low cost. Thus, developing reliable non-destructive testing (NDT) methods for quality assurance of components made by these materials is an important step necessary for their widespread use in critical applications.

One of the commonly used NDT methods for non-metallic materials is ultrasonic testing [1][2]. Due to the complex structure of composite materials such as FRP/GRE [3], nature of defects, and failure morphology particularly in HDPE thermal fusion joints, ultrasonic testing fails to perform NDT for these materials [4][5]. Another common NDT method is radiography which relies on the use of X-ray [6]. In addition to extra safety requirements, radiography is not capable of detecting delaminations and planar cracks since for such defects the local density remains almost the same.

To address the above-mentioned shortcomings of the traditional NDT methods for inspection of non-metallic components, microwave measurements have been proposed (e.g., see [7], [8]). So far, microwave NDT techniques proposed for imaging of cylindrical dielectric materials can be divided into two groups: imaging based on raw responses and imaging based on synthetic aperture radar (SAR) processing. Regarding the first group, in [9]-[12], two dimensional (2D) imaging has been performed using scalar measurements only. In [13], a K-band (18–26.5 GHz) microwave reflectometry system employing an in-line crawling robot has been proposed, which is capable of providing 2D images of cracks in HDPE pipes. Regarding the second group, in [14], wideband millimeter wave SAR imaging has been employed to produce three-dimensional (3D) images of vertical cracks/flaws in flat and curved HDPE pipes. There, a portable and low cost Ka-band (26.5–40 GHz) reflectometer with a single antenna has been proposed for the measurements. In [15], a SAR-based NDT method for multilayered pipes has been proposed in *X*-band (8.2–12.4 GHz). There, a closed-form Green's function has been employed which accounts for the different propagation delays, internal reflections, and refractions, and the image reconstruction process is based on the use of matched filter. In [16], time-reversal SAR imaging has been proposed for inspections of lossy symmetric and asymmetric layered dielectric cylindrical objects in *X*-band (8.2–12.4 GHz). There, the transmission and refraction path at the boundaries between different layers have been considered. In [17], an algorithm has been proposed to improve SAR imaging for insulated steel pipes using X-band (8.2–12.4 GHz), Ku-band (12.4−18 GHz), and K-band (18−26.5 GHz). It is based on autofocus range-Doppler algorithm and singular value decomposition has been used to mitigate the effect of the insulation layer.

Recently, SAR imaging (in the far-field, SAR imaging is equivalent to direct holographic imaging [18]) has been extended to near-field 2D [19] and 3D imaging [20]-[23]. These techniques are commonly referred to as near-field holographic imaging techniques. In the latest developments [18], [23], the information related to the incident field and the Green's function for a specific imaging system is obtained via the measurement of the point-spread function (PSF) of the imaging system. In practice, this allows for: (1) achieving sub-diffraction resolution due to the use of measurable parts of the

H. Wu, M. Ravan, J. Patel, and R. K. Amineh are with the Department of Electrical and Computer Engineering, New York Institute of Technology, New York, NY 10023, USA (Corresponding author: R. K. Amineh, e-mail: rkhalaja@nyit.edu).

R. Sharma was with the Department of Electrical and Computer Engineering, New York Institute of Technology, New York, NY 10023, USA. She is now with the Electro-Metrics Corporation, Johnstown, NY 12095 USA.

evanescent wave spectrum in the near-field instead of using far-field analytical terms, (2) reducing the modeling errors as the antennas and the imaging setup are not required to be modeled, (3) reducing errors due to the uncertainties of the material properties since the PSFs are obtained via measurements instead of using pre-determined material property values and analytical expressions, (4) reducing errors due to the size of antennas since they directly measure the PSFs instead of assuming point-wise antennas. While it is still possible to use analytical expressions for the PSF in the proposed technique, the uncertainty in the material properties or the ignored near-field terms can slightly degrade the quality of the reconstructed images.

In this paper, a near-field holographic microwave imaging technique is proposed to provide images of multiple concentric pipes. Such configuration is commonly used in various industries, to improve the efficiency and increase the lifetime of the wellbore production pipes in oil and gas industry [24] or to separate the flow in the fluid transfer pipeline [25]. The use of cylindrical setups for pipe imaging necessitates modifications in the image reconstruction methods in near-field microwave holographic imaging due to the periodic nature of the scattered fields along the azimuthal direction (e.g., see [26]-[28]). Here, an array of receiver antennas are employed which allows for using the narrowest possible frequency band. In fact, the use of antenna array allows for data collection over diverse positions that, in turn, allows for achieving range (radial) resolution [29]. Although the pipes may not be highly dispersive, they may carry dispersive fluids. In such case, using a narrower band allows for reducing the imaging errors due to the dispersion. Furthermore, the use of a narrow band system allows for using resonant antennas which improves the dynamic range of the imaging system (resonant antennas are more sensitive to the changes of the materials around them at their resonant frequency which allows for detecting smaller defects). Another main development, here, is the solution of systems of equations in the near-field holographic imaging based on the use of standardized minimum norm (SMN) approach which alleviates the depth biasing problem. The performance of the proposed imaging technique is studied, first, via simuations and then through experiments with double PVC pipes with two different placements of the antenna array: outside the pipes and inside the pipes.

II. Theory of Holographic Imaging for Non-Metallic Pipes

In this section, we introduce the theory of near-field holographic imaging with an array of receiver antennas and multiple frequency data for imaging the defects in non-metallic concentric pipes. Unlike the previous near-field microwave holographic imaging studies based on rectangular setups [20]-[23], in pipe imaging, the data acquisition and image reconstruction need to be performed over cylindrical surfaces (along azimuthal and longitudinal directions) at various radii. Thus, all the functions are periodic versus azimuthal direction (ϕ). This necessitates the use of circular deconvolution method that will be discussed as follows.

Fig. 1 illustrates the proposed microwave imaging setup including a transmitter antenna to illuminate pipes and an array of N_A receiver antennas that scans the scattered fields. The transmitter antenna and the array of receiver antennas scan a cylindrical aperture with radius of r_A and height of z_A. The scattered field is recorded at N_ϕ angles along the azimuthal direction ϕ (within [0, 2π]) and N_z positions along the longitudinal direction z. The complex-valued scattered field, $E^{SC}(\phi,z)$, is measured, at each sampling position, at N_ω frequencies within the band of ω_1 to ω_{N_ω}, by each receiver. Such scattered response is obtained from subtracting the response of the pipes without defects from the response of the same pipes with defects. The image reconstruction process then provides images of the pipes with radii r_i , where $i=1,\ldots,N_r$. It is worth noting that the imaging system is assumed to be linear and space-invariant (LSI). The use of Born approximation for the scattering integral leads to the linear property of the imaging system [20].

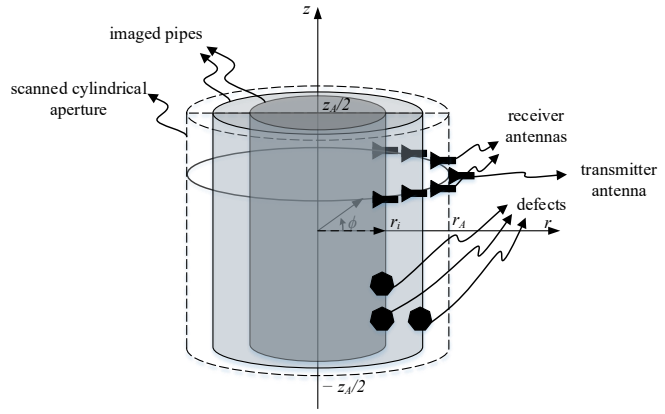

Fig. 1. Illustration of the microwave imaging setup. A transmitter antenna and an array of receiver antennas scan a cylindrical aperture and the images are reconstructed over cylindrical surfaces with radii r=r_i.

For implementation of the holographic imaging, first, the point-spread functions (PSFs) of the LSI imaging system are acquired. These PSFs are denoted by $E^{SC,CD}$ and are approximated by measuring small defects called calibration defects (CDs) placed on each pipe one at a time. The scattered response recorded for a CD placed on the *i*-th pipe is denoted by $E_i^{SC,CD}(\phi,z)$. The defects' response for each pipe, $E_i^{SC}(\phi,z)$, can be written, according to the convolution theory, as the convolution of the collected PSF for that pipe, $E_i^{SC,CD}(\phi,z)$, with the contrast function of the defect on the corresponding pipe $f_i(\phi,z)$. Then, the response due to the defects on all the pipes under test (PUTs), $E^{SC}(\phi,z)$, can be obtained from the superposition of the responses of all the pipes, $E_i^{SC}(\phi,z)$, where $i=1,\ldots,N_r$, as:

This article has been accepted for publication in a future issue of this journal, but has not been fully edited. Content may change prior to final publication. Citation information: DOI 10.1109/TIM.2020.2980340, IEEE Transactions on Instrumentation and Measurement

$$E^{SC}(\phi,z)=\sum_{i=1}^{N_r}E_i^{SC}(\phi,z)=\sum_{i=1}^{N_r}E_i^{SC,CD}(\phi,z)*_\phi *_z f_i(\phi,z) \quad (1)$$

$*_\phi$ and $*_z$ denote for convolutions along ϕ and z, respectively. In Eq. (1), PSF functions, $E_i^{SC,CD}(\phi,z)$, can be obtained *a priori* via measurement or simulation. Besides, $E^{SC}(\phi,z)$ is obtained by recording the responses for the defects on PUTs. The goal is then to estimate the contrast functions of the defects $f_i(\phi,z)$. The contrast function of defect, $f_i(\phi,z)$, relates to the wavenumbers of defected region (air or fluid), k_s, and background medium (pipe), k_b, as [23]:

$$f_i(\phi,z)=k_s^2(\phi,z)-k_b^2(\phi,z) \quad (2)$$

To provide more data for image reconstcrution, measurements can be implemented at multiple frequencies (over the narrowest possible band), ω_n, n=1,…, N_ω and by multiple receivers, a_m, m=1,…, N_A. Thus, for each receiver a_m, Eq. (1) can be re-written at all frequencies to provide the following system of equations:

$$\begin{cases} E_{a_m}^{SC}(\phi,z,\omega_1)=\sum_{i=1}^{N_r}E_{i,a_m}^{SC,CD}(\phi,z,\omega_1)*_\phi *_z f_i(\phi,z) \\ \vdots \\ E_{a_m}^{SC}(\phi,z,\omega_{N_\omega})=\sum_{i=1}^{N_r}E_{i,a_m}^{SC,CD}(\phi,z,\omega_{N_\omega})*_\phi *_z f_i(\phi,z) \end{cases} \quad (3)$$

The systems of equations written for all the receivers a_m, m=1,…, N_A, can be combined to find the shared unknown parameters $f_i(\phi,z)$, $i=1,\dots,N_r$. In order to solve the system of equations, we apply Fourier Transform (FT) on both sides of the equations.

Let's first consider the spatially-sampled versions of $E_{a_m}^{SC}(\phi,z,\omega_n)$, $E_{i,a_m}^{SC,CD}(\phi,z,\omega_n)$, and $f_i(\phi,z)$ denoted by $\mathbf{E}_{a_m}^{SC}(n_\phi,n_z,\omega_n)$, $\mathbf{E}_{i,a_m}^{SC,CD}(n_\phi,n_z,\omega_n)$, and $\mathbf{f}_i(n_\phi,n_z)$, $n_\phi=1,...,N_\phi$ and $n_z=1,\dots,N_Z$, with spatial and angular intervals denoted by Δz and $\Delta\phi$, respectively. Then, the convolutions in Eq. (1) can be written in spectral domain as [30]:

$$\begin{aligned}&\mathrm{DTFT}_{z,\phi}\{\mathbf{E}_{a_m}^{SC}(n_\phi,n_z,\omega_n)\}=\\&\sum_{i=1}^{N_r}\mathrm{DTFT}_{z,\phi}\{\mathbf{E}_{i,a_m}^{SC,CD}(n_\phi,n_z,\omega_n)\}\mathrm{DTFT}_{z,\phi}\{\mathbf{f}_i(n_\phi,n_z)\}\end{aligned} \quad (4)$$

where $\mathrm{DTFT}_{z,\phi}$ denotes discrete time FT (DTFT) along azimuthal and longitudinal directions, respectively. Sequences $\mathbf{E}_{a_m}^{SC}(n_\phi,n_z,\omega_n)$, $\mathbf{E}_{i,a_m}^{SC,CD}(n_\phi,n_z,\omega_n)$, and $\mathbf{f}_i(n_\phi,n_z)$ are aperiodic along the longitudinal direction z. The DTFTs with respect to z are denoted by $\tilde{\mathbf{E}}_{a_m}^{SC}(n_\phi,k_z,\omega_n)$, $\tilde{\mathbf{E}}_{i,a_m}^{SC,CD}(n_\phi,k_z,\omega_n)$, and $\tilde{\mathbf{f}}_i(n_\phi,k_z)$. Since these functions are periodic along ϕ, the convolution along that direction can be considered as a circular convolution [30]. Then, the DTFTs for the N_ϕ-periodic sequences along ϕ are computationally reduced to discrete Fourier transforms (DFT) of these sequences [30]. The DFTs with respect to the ϕ variable for sequences $\tilde{\mathbf{E}}_{a_m}^{SC}(n_\phi,k_z,\omega_n)$, $\tilde{\mathbf{E}}_{i,a_m}^{SC,CD}(n_\phi,k_z,\omega_n)$, and $\tilde{\mathbf{f}}_i(n_\phi,k_z)$ are denoted by $\tilde{\tilde{\mathbf{E}}}_{a_m}^{SC}(k_\phi,k_z,\omega_n)$, $\tilde{\tilde{\mathbf{E}}}_{i,a_m}^{SC,CD}(k_\phi,k_z,\omega_n)$, and $\tilde{\tilde{\mathbf{f}}}_i(k_\phi,k_z)$, where k_ϕ is an integer from 0 to $N_\phi-1$.

Using the transformations discussed above at all the frequencies for each receiver a_m leads to the following system of equations at each spatial frequency pair $\boldsymbol{\kappa}=(k_\phi,k_z)$:

$$\begin{cases} \tilde{\tilde{\mathbf{E}}}_{a_m}^{SC}(\boldsymbol{\kappa},\omega_1)=\sum_{i=1}^{N_r}\tilde{\tilde{\mathbf{E}}}_{i,a_m}^{SC,CD}(\boldsymbol{\kappa},\omega_1)\tilde{\tilde{\mathbf{f}}}_i(\boldsymbol{\kappa}) \\ \vdots \\ \tilde{\tilde{\mathbf{E}}}_{a_m}^{SC}(\boldsymbol{\kappa},\omega_{N_\omega})=\sum_{i=1}^{N_r}\tilde{\tilde{\mathbf{E}}}_{i,a_m}^{SC,CD}(\boldsymbol{\kappa},\omega_{N_\omega})\tilde{\tilde{\mathbf{f}}}_i(\boldsymbol{\kappa}) \end{cases} \quad (5)$$

By merging the systems of equations for all the N_A receivers, the following system of equations is obtained at each spatial frequency pair $\boldsymbol{\kappa}=(k_\phi,k_z)$:

$$\underline{\tilde{\tilde{\mathbf{E}}}}^{SC}=\underline{\underline{\tilde{\tilde{\mathbf{D}}}}}\,\underline{\tilde{\tilde{\mathbf{F}}}} \quad (6)$$

where

$$\underline{\tilde{\tilde{\mathbf{E}}}}^{SC}=\begin{bmatrix}\underline{\tilde{\tilde{\mathbf{E}}}}_1^{SC}\\ \vdots \\ \underline{\tilde{\tilde{\mathbf{E}}}}_{N_A}^{SC}\end{bmatrix},\ \underline{\underline{\tilde{\tilde{\mathbf{D}}}}}=\begin{bmatrix}\underline{\tilde{\tilde{\mathbf{D}}}}_1\\ \vdots \\ \underline{\tilde{\tilde{\mathbf{D}}}}_{N_A}\end{bmatrix},\ \underline{\tilde{\tilde{\mathbf{F}}}}=\begin{bmatrix}\tilde{\tilde{\mathbf{f}}}_1(\boldsymbol{\kappa})\\ \vdots \\ \tilde{\tilde{\mathbf{f}}}_{N_r}(\boldsymbol{\kappa})\end{bmatrix} \quad (7)$$

and

$$\underline{\tilde{\tilde{\mathbf{E}}}}_{a_m}^{SC}=\begin{bmatrix}\tilde{\tilde{\mathbf{E}}}_{a_m}^{SC}(\boldsymbol{\kappa},\omega_1)\\ \vdots \\ \tilde{\tilde{\mathbf{E}}}_{a_m}^{SC}(\boldsymbol{\kappa},\omega_{N_\omega})\end{bmatrix},$$

$$\underline{\underline{\tilde{\tilde{\mathbf{D}}}}}_{a_m}=\begin{bmatrix}\tilde{\tilde{\mathbf{E}}}_{1,a_m}^{SC,CD}(\boldsymbol{\kappa},\omega_1) & \cdots & \tilde{\tilde{\mathbf{E}}}_{N_r,a_m}^{SC,CD}(\boldsymbol{\kappa},\omega_1)\\ \vdots & \ddots & \vdots \\ \tilde{\tilde{\mathbf{E}}}_{1,a_m}^{SC,CD}(\boldsymbol{\kappa},\omega_{N_\omega}) & \cdots & \tilde{\tilde{\mathbf{E}}}_{N_r,a_m}^{SC,CD}(\boldsymbol{\kappa},\omega_{N_\omega})\end{bmatrix} \quad (8)$$

These systems of equations are solved at each spatial frequency pair $\boldsymbol{\kappa}=(k_\phi,k_z)$ to obtain the values for $\tilde{\tilde{\mathbf{f}}}_i(\boldsymbol{\kappa})$, $i=1,\dots,N_r$. Then, inverse DTFT along longitudinal direction z and inverse DFT along azimuthal direction ϕ are applied to reconstruct images, $\mathbf{f}_i(n_\phi,n_z)$, over all the pipes with radii $r=r_i$, $i=1,\dots,N_r$. At the end, the normalized modulus of $\mathbf{f}_i(n_\phi,n_z)$, $|\mathbf{f}_i(n_\phi,n_z)|/M$, where M is the maximum of

$|\mathbf{f}_i(n_\phi, n_z)|$ for all r_i, is plotted versus ϕ and z to obtain a 2D image of the defects on the *i*-th pipe. We call $|\mathbf{f}_i(n_\phi, n_z)|/M$ the normalized image.

III. Solution of the Systems of Equations with Standardized Minimum Norm Approach

The common approach to solve the systems of equations in near-field holographic imaging is the well-known minimum norm (MN) solution [20]-[23]. However, the MN solution is notorious for depth biasing, i.e., underestimation of deep features in favor of ones that are more superficial. Here, this leads to only detection of the defects that are closer to the antennas. In this project, inspired by standardized low-resolution brain electromagnetic tomography using EEG data [31], we study the improvements gained via standardization of the minimum norm inverse solution. Using this concept, the objective function to be minimized is constructed as:

$$J = \left\| \underline{\underline{\tilde{\tilde{\mathbf{E}}}}}^{SC} - \underline{\underline{\tilde{\tilde{\mathbf{D}}}}} \underline{\underline{\tilde{\tilde{\mathbf{F}}}}} \right\|^2 + \alpha \left\| \underline{\underline{\tilde{\tilde{\mathbf{F}}}}} \right\| \tag{9}$$

where $\alpha \geq 0$ is a regularization parameter. This parameter is taken as the variance of the noise in the simulated or measured data. Here, we estimate the noise variance by minimizing the generalized cross-validation (GCV) score [32] using MATLAB command *evar*. In this method, it is assumed that the value for which the GCV score is minimal can provide the variance of the additive noise. The functional *J* is to be minimized with respect to $\underline{\underline{\tilde{\tilde{\mathbf{F}}}}}$, for given $\underline{\underline{\tilde{\tilde{\mathbf{D}}}}}$, $\underline{\underline{\tilde{\tilde{\mathbf{E}}}}}^{SC}$, and α. The explicit solution to this minimization problem is:

$$\underline{\underline{\hat{\tilde{\tilde{\mathbf{F}}}}}} = \mathbf{P} \underline{\underline{\tilde{\tilde{\mathbf{E}}}}}^{SC} \tag{10}$$

where

$$\mathbf{P} = \underline{\underline{\tilde{\tilde{\mathbf{D}}}}}^{\mathrm{H}} \mathbf{L} \left[\mathbf{L} \underline{\underline{\tilde{\tilde{\mathbf{D}}}}} \underline{\underline{\tilde{\tilde{\mathbf{D}}}}}^{\mathrm{H}} \mathbf{L} + \alpha \mathbf{L} \right]^{+}, \tag{11}$$

$\underline{\underline{\hat{\tilde{\tilde{\mathbf{F}}}}}}$ is the estimate of $\underline{\underline{\tilde{\tilde{\mathbf{F}}}}}$, $\mathbf{L}_{N_\omega N_A \times N_\omega N_A} = \mathbf{I} - \mathbf{1}\mathbf{1}^{\mathrm{T}} / \mathbf{1}^{\mathrm{T}}\mathbf{1}$ denotes the centering matrix, $\mathbf{I}_{N_\omega N_A \times N_\omega N_A}$ is the identity matrix, $\mathbf{1}_{N_\omega N_A \times 1}$ is a vector of ones, $[\cdot]^{\mathrm{H}}$ is Hermitian transpose operation, and $[\cdot]^{+}$ denotes Moore-Penrose pseudoinverse. Standardization of the estimate $\underline{\underline{\hat{\tilde{\tilde{\mathbf{F}}}}}}$ requires an estimate of its variance. The true variance of $\underline{\underline{\tilde{\tilde{\mathbf{F}}}}}$ is equal to the identity matrix but this is for an ideal case when $\underline{\underline{\tilde{\tilde{\mathbf{F}}}}}$ is estimated without error. Thus, in reality, to obtain variance of $\underline{\underline{\hat{\tilde{\tilde{\mathbf{F}}}}}}$ denoted by $\mathbf{S}_{\underline{\underline{\hat{\tilde{\tilde{\mathbf{F}}}}}}}$, from (10), we have:

$$\mathbf{S}_{\underline{\underline{\hat{\tilde{\tilde{\mathbf{F}}}}}}} = \mathbf{P} \mathbf{S}_{\underline{\underline{\tilde{\tilde{\mathbf{E}}}}}^{SC}} \mathbf{P}^{\mathrm{H}} \tag{12}$$

where $\mathbf{S}_{\underline{\underline{\tilde{\tilde{\mathbf{E}}}}}^{SC}}$ is the variance of $\underline{\underline{\tilde{\tilde{\mathbf{E}}}}}^{SC}$ from the Bayesian point of view and it is due to the noisy measurements. Assuming independence of $\underline{\underline{\tilde{\tilde{\mathbf{F}}}}}$ and measurement noise, $\mathbf{S}_{\underline{\underline{\tilde{\tilde{\mathbf{E}}}}}^{SC}}$ can be written as:

$$\mathbf{S}_{\underline{\underline{\tilde{\tilde{\mathbf{E}}}}}^{SC}} = \underline{\underline{\tilde{\tilde{\mathbf{D}}}}} \underline{\underline{\tilde{\tilde{\mathbf{D}}}}}^{\mathrm{H}} + \mathbf{S}_{\underline{\underline{\tilde{\tilde{\mathbf{E}}}}}^{SC}}^{noise} = \underline{\underline{\tilde{\tilde{\mathbf{D}}}}} \underline{\underline{\tilde{\tilde{\mathbf{D}}}}}^{\mathrm{H}} + \alpha \mathbf{L} \tag{13}$$

Therefore, from (12) and (13), the variance of $\underline{\underline{\hat{\tilde{\tilde{\mathbf{F}}}}}}$ is

$$\mathbf{S}_{\underline{\underline{\hat{\tilde{\tilde{\mathbf{F}}}}}}} = \mathbf{P} \left(\underline{\underline{\tilde{\tilde{\mathbf{D}}}}} \underline{\underline{\tilde{\tilde{\mathbf{D}}}}}^{\mathrm{H}} + \alpha \mathbf{L} \right) \mathbf{P}^{\mathrm{H}} = \underline{\underline{\tilde{\tilde{\mathbf{D}}}}}^{\mathrm{H}} \left(\underline{\underline{\tilde{\tilde{\mathbf{D}}}}} \underline{\underline{\tilde{\tilde{\mathbf{D}}}}}^{\mathrm{H}} + \alpha \mathbf{L} \right)^{+} \underline{\underline{\tilde{\tilde{\mathbf{D}}}}} \tag{14}$$

The standardization of $\underline{\underline{\hat{\tilde{\tilde{\mathbf{F}}}}}}$ is then estimated as [33]:

$$\underline{\underline{\hat{\tilde{\tilde{\mathbf{F}}}}}} = \sqrt{(\mathrm{Diag}(\mathbf{S}_{\underline{\underline{\hat{\tilde{\tilde{\mathbf{F}}}}}}}))^{-1}} \mathbf{P} \underline{\underline{\tilde{\tilde{\mathbf{E}}}}}^{SC} \tag{15}$$

where $\mathrm{Diag}(\mathbf{S}_{\underline{\underline{\hat{\tilde{\tilde{\mathbf{F}}}}}}})$ is the diagonal matrix formed by the diagonal elements of $\mathbf{S}_{\underline{\underline{\hat{\tilde{\tilde{\mathbf{F}}}}}}}$.

IV. Simulation Results

To study the performance of the proposed imaging technique, here, the capabilities and limitations of single frequency imaging is studied via simulations based on FEKO software. To expedite the study, the scanning and image reconstructions are performed one-dimensionally along the azimuthal direction at the operation frequency of 10 GHz.

A. Circular Scanning and Image Reconstruction with Antenna Array Outside the Pipes

In this section, we study the performance of the system when the antenna array is placed outside the pipes. In a *reference setup*, we use an array of 13 dipole antennas, as illustrated in Fig. 2, separated at $\Delta\phi_a$ = 10° angles along the ϕ direction (azimuth angles) and scanning at R_a = 50 mm from the center. The center element is excited while the rest of the antennas are used as the receivers. The radii of the inner and outer pipes R_{out1} and R_{out2} are 20 mm and 40 mm respectively. The thickness of both pipes is D = 2 mm. There are two defects on the outer pipe centered at $\phi = 10°$ and $-10°$ ($\Delta\phi_d = 20°$ in Fig. 2), and one defect on the inner cylinder centered at $\phi = 0°$. All defects have the same shape and size. They are semi-cylindrical with radius of 0.75D (with reference to Fig. 2, $W_d = 0.75D$ and $L_d = 1.5D$). Table I shows the values of the parameters for this *reference setup*. The pipes have a relative permittivity ε_r of 2.25 and loss tangent of 0.0004.

In FEKO, we perform the scanning of a circular aperture to get the complex-valued *S*-parameters by rotating the antenna(s) along the azimuth angle (ϕ) from 0° to 360° in 181 grid points (every 2°). To have a realistic simulation study, white Gaussian noise with signal-to-noise ratio (SNR) of 20 dB is added to the data using the *awgn* commend in MATLAB by which the signal level is computed first, to determine the appropriate noise level based on the value of SNR.

First, we perform a simulation of the pipes without the

This article has been accepted for publication in a future issue of this journal, but has not been fully edited. Content may change prior to final publication. Citation information: DOI 10.1109/TIM.2020.2980340, IEEE Transactions on Instrumentation and Measurement

presence of any defect to obtain the background responses. These responses are then subtracted from the responses simulated in the presence of the defects on the pipes to obtain the scattered responses. Then, holographic imaging is applied on the scattered responses. Fig. 3 shows the reconstructed images for the outer and inner pipes. It is observed that when using holographic imaging with SMN approach compared to MN approach, the quality of the reconstructed images drastically improves, in particular, for the inner pipe as expected. We can clearly detect the defects at their true locations on both pipes after applying holographic imaging with SMN approach. We estimate the resolutions of the images in the azimuthal direction. The resolution evaluation is implemented based on the 3-dB level (half-power level) as it is common in the diffraction limited systems (e.g., see [34], [35]). Thus, it is the distance between two points marking 0.7 times the peak value. Resolutions are found to be approximately 4.8 mm and 3.4 mm for the outer and inner pipes, respectively.

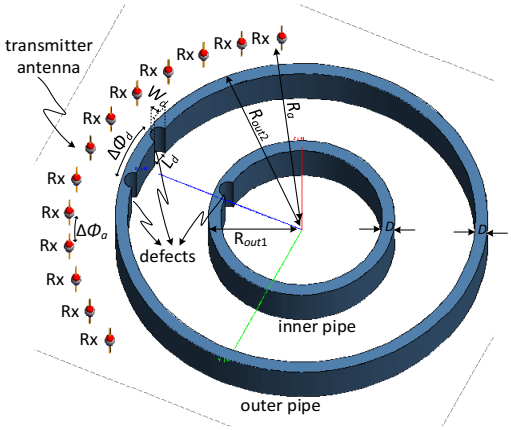

Fig. 2. Illustration of FEKO simulation setup consisting of N_A receiver antennas and one transmitter antenna with angular separation of $\Delta\phi_a$ scanning outside the pipes at radius of R_a along the azimuthal direction. The two pipes have radii of R_{out1} and R_{out2}. The thickness of the pipes is D. The outer pipe has two defects with angular separation of $\Delta\phi_d$, opening of L_d, and depth of W_d. The inner pipe has one defect with the same size.

TABLE I
PARAMETER VALUES FOR THE SETUP IN FIG. 2 (*REFERENCE SETUP*)

N_A	$\Delta\phi_a$	R_a	R_{out1}	R_{out2}	D	L_d	W_d	$\Delta\phi_d$
12	10°	50 mm	20 mm	40 mm	2 mm	1.5D	0.75D	20°

In the following, we study the effects of some of the most important parameters. To evaluate the quality of the reconstructed images, we define a reconstruction error parameter E_T as:

$$E_T = \sum_{i=1}^{N_r} \left\| \mathbf{f}_i(n_\phi, n_z) \right| / M - \mathbf{f}_{i,ideal}(n_\phi, n_z) \right\| \qquad (16)$$

where $\mathbf{f}_{i,ideal}(n_\phi, n_z)$ is the ideal image for which the values are all 0 except being 1 at the true positions of the defects.

First, we study the effect of standoff distance R_a for the antenna. We record the responses when the antennas are scanning the pipes at R_a = 51 mm and 52 mm (instead of R_a = 50 mm in the *reference setup*) and we reconstruct images with the PSFs obtained for R_a = 50 mm. Fig. 4 shows the reconstructed images for R_a = 52 mm. Also, Table II compares the values of the reconstruction error for these various standoff distances. It is observed that the quality of the images degrades with the error in the standoff distance. The degradation less severe when using SMN approach.

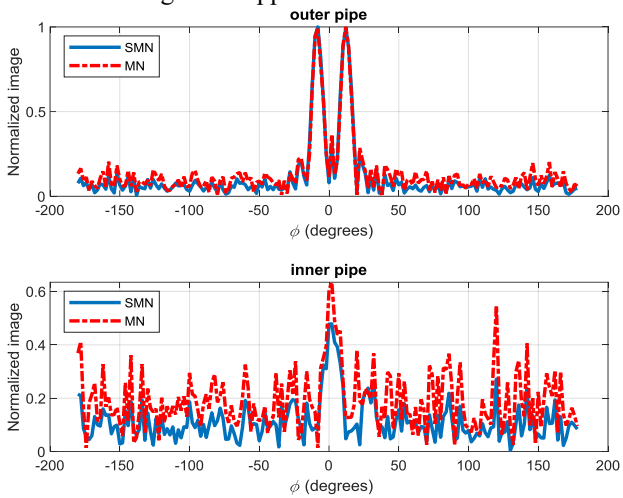

Fig. 3. Reconstructed images in case of N_A = 12 dipole receiver antennas separated $\Delta\phi_a$ = 10° from each other at a distance of R_a = 50 mm from the center. For this example, the parameters are R_{out1} = 20 mm, R_{out2} = 40 mm, D = 2 mm, and SNR = 20 dB.

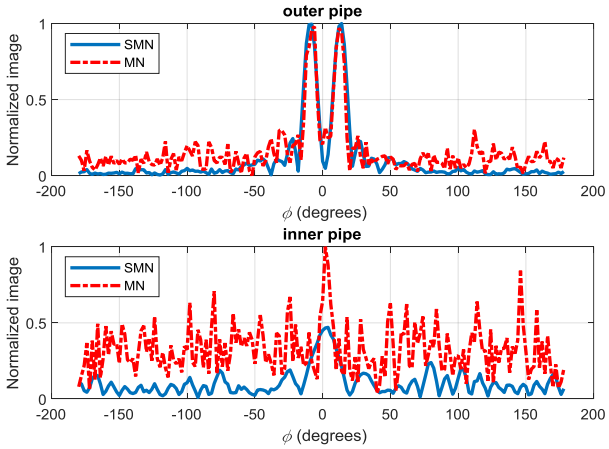

Fig. 4. Reconstructed images when parameters are the same as those for the *reference setup* except that R_a = 52 mm.

TABLE II
VARIATION OF E_T FOR VARIOUS STANDOFF DISTANCES

R_a (mm)	50	51	52
E_T(MN)	2.63	3.08	3.53
E_T(SMN)	2.15	2.19	2.23

Next, to study the effect of number of antennas, we reconstruct images using data collected by only N_A = 4 or 8 antennas (instead of N_A = 12 in the *reference setup*). Fig. 5 shows the reconstructed images when using 4 receiver antennas and Table III shows the reconstruction error when using N_A = 4, 8, and 12 receiver antennas. It is observed that the error increases with the decrease in the number of employed receiver antennas. The degradation less severe when using SMN approach.

Then, to study the effect of the angular separation between

This article has been accepted for publication in a future issue of this journal, but has not been fully edited. Content may change prior to final publication. Citation information: DOI 10.1109/TIM.2020.2980340, IEEE Transactions on Instrumentation and Measurement

the antennas, we study the *reference setup* with different $\Delta\phi_a$ values. Fig. 6 shows the reconstructed images for 12 receiver antennas with $\Delta\phi_a = 7°$ and Table IV shows the reconstruction errors for various angular separations between the antennas $\Delta\phi_a$ ($\Delta\phi_a = 27°$ corresponds to the case that the antennas distribute almost uniformly over the full circle). It is observed that when using MN approach, increasing $\Delta\phi_a$ from 7° to 10° leads to the decrease in the E_T. This is due to the fact that by increasing $\Delta\phi_a$, information is collected over more diverse positions where the responses of the defects are strong. But there is a limit for the improvement in E_T with the increase of $\Delta\phi_a$. This is due to the weaker receiver responses for larger values of $\Delta\phi_a$ (larger than the limit discussed above) compromising the effect of collecting information in diverse positions. Very large angular separation between the receiver antennas, in fact, increases the overall travel path of the waves from transmitter to receivers via defects (transmitter-defect path plus defect-receiver path). When using SMN approach, with increasing $\Delta\phi_a$ from 10° to 27°, the values of E_T do not vary much.

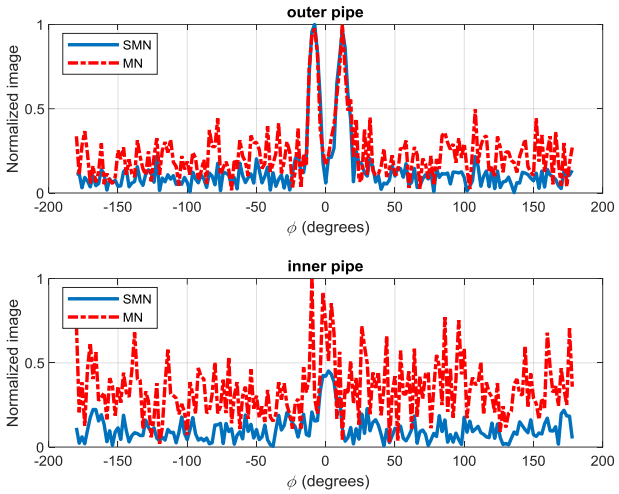

Fig. 5. Reconstructed images when parameters are the same as those for the *reference setup* except that $N_A = 4$.

TABLE III
VARIATION OF E_T FOR VARIOUS NUMBER OF RECEIVER ANTENNAS

N_A (mm)	4	8	12
E_T(MN)	4.14	3.51	2.63
E_T(SMN)	2.37	2.21	2.15

Next, to study the effect of thickness of the imaged pipes, we increase the thickness of the pipes in the *reference setup* to D = 5 mm and 7 mm. Fig. 7 shows the reconstructed images for D = 5 mm. Also, Table V shows the computed values for E_T for D = 5 mm and 7 mm. It is observed that the value of E_T increases with the increase of D when using both MN and SMN approaches. To study the possible reason for image quality deterioration, we performed the simulations on lossless pipes ($\tan\delta = 0$) using the same parameters for the case shown in Fig. 7. The reconstructed images of the defects on two lossless pipes have better quality than the ones in Fig. 7, as deduced from comparison of reconstruction errors in Table V. Thus, one of the reasons for the deterioration of the images for larger pipe thicknesses is due to the wave attenuation. Besides, it is observed that the quality of the images for lossless pipes with D = 5 mm is still lower when using MN approach compared to the one with D = 2 mm. We believe that another reason for this quality deterioration is the stronger multiple scattering between the pipes for larger pipe thicknesses.

Last, in order to study the range (radial) resolution, we perform image reconstructions with various R_{out1} while keeping R_{out2} = 40 mm. Fig. 8 shows the reconstructed images when R_{out1} = 37 mm (1 mm gap between the two pipes). Also, Table VI shows the variation of the E_T when the gap between the two

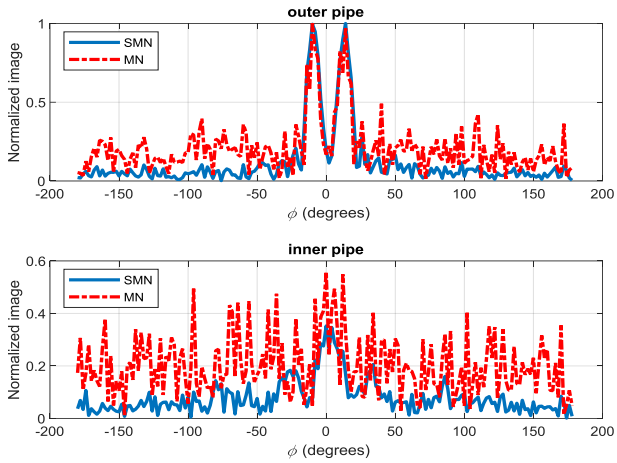

Fig. 6. Reconstructed images when parameters are the same as those for the *reference setup* except that $\Delta\phi_a = 7°$.

TABLE IV
VARIATION OF E_T FOR VARIOUS ANGULAR SEPARATION BETWEEN ANTENNAS

$\Delta\phi_a$ (°)	7	10	15	27
E_T(MN)	3.12	2.63	2.89	2.98
E_T(SMN)	2.36	2.15	2.14	2.12

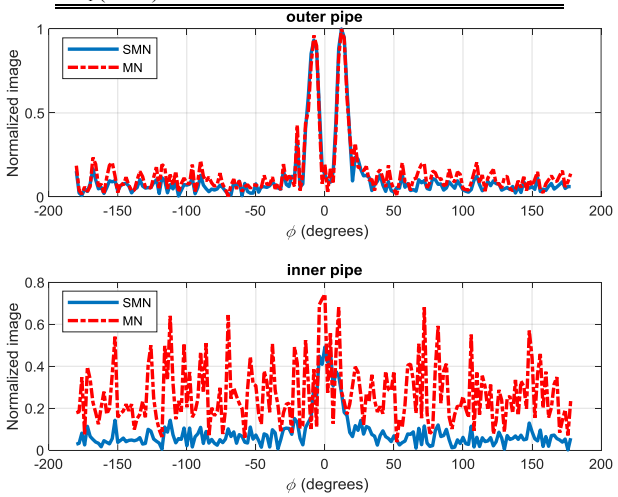

Fig. 7. Reconstructed images when parameters are the same as those for the *reference setup* except that D = 5 mm.

TABLE V
VARIATION OF E_T FOR VARIOUS PIPE THICKNESSES

D (mm)	2	5	5 ($\tan\delta = 0$)	7
E_T(MN)	2.63	3.32	3.24	3.38
E_T(SMN)	2.15	2.17	2.02	2.41

This article has been accepted for publication in a future issue of this journal, but has not been fully edited. Content may change prior to final publication. Citation information: DOI 10.1109/TIM.2020.2980340, IEEE Transactions on Instrumentation and Measurement

pipes decreases. It is observed that, when R_{out1} varies from 20 mm to 30 mm (as the inner pipe is getting closer to the antenna array), the value of E_T decreases for both MN and SMN approaches due to the stronger signal recorded by the receiver antennas for the defects on the inner pipe. Besides, although all of the defects are still resolvable in Fig. 8, for the smallest gap between the two pipes (R_{out1} = 37 mm) the values of E_T increase for both MN and SMN approaches compared to the case in which R_{out1} = 30 mm. According to our study, the reason is that, for R_{out1} = 37 mm, the columns of matrix of coefficients $\tilde{\tilde{\mathbf{D}}}$ for the system of equations in (6) become more correlated, leading to larger condition number and more erroneous solution.

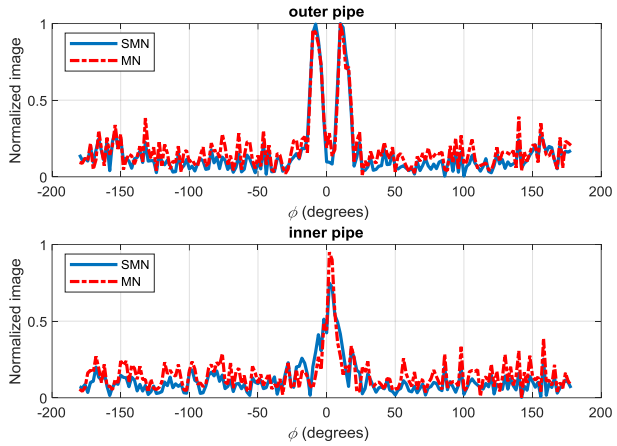

Fig. 8. Reconstructed images when parameters are the same as those for the *reference setup* except that R_{out1} = 37 mm.

TABLE VI
VARIATION OF E_T FOR VARIOUS RADII OF THE INNER PIPE

R_{out1} (mm)	20	30	37
E_T (MN)	2.63	2.34	2.75
E_T (SMN)	2.15	1.99	2.39

B. Circular Scanning and Image Reconstruction with Antenna Array Inside the Pipes

In this section, we study the performance of the system when the antenna array is placed inside the pipes. We use an array of 9 dipole antennas with angular separation of $\Delta\phi_a$ = 30° and scanning at the radius of R_a = 47 mm, as illustrated in Fig. 9. The center antenna is excited while the rest are receivers. The radii of the inner and outer pipes R_{out1} and R_{out2} are 57.5 mm and 79 mm, respectively. The pipes have a thickness of D = 2 mm. There are two defects on the outer pipe centered at $\phi = 10°$ and $-10°$ ($\Delta\phi_d = 20°$ in Fig. 9), and one defect on the inner pipe centered at $\phi = 0°$. All defects have the same shape and size. They are semi-cylindrical with radius of 0.75D (with reference to Fig. 9, $W_d = 0.75D$ and $L_d = 1.5D$). Table II shows the values of the parameters for the setup. The pipes are with relative permittivity ε_r of 2.25 and loss tangent of 0.0004.

In FEKO, we perform the scanning of a circular aperture to get the complex-valued S-parameters by rotating the antenna(s) along the azimuth angle (ϕ) from 0° to 360° in 181 grid points (every 2°). To have a realistic simulation study, additive White

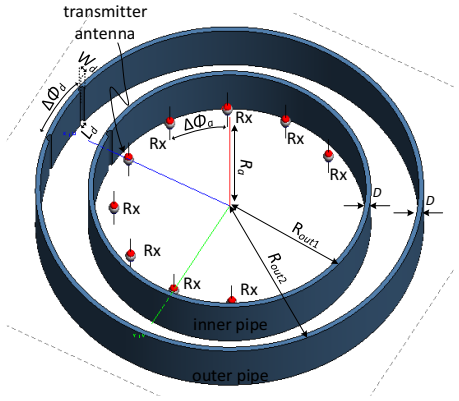

Fig. 9. Illustration of FEKO simulation setup consisting of N_A dipole receiver antennas and one transmitter antenna with angular separation of $\Delta\phi_a$ scanning inside the pipes at radius of R_a along the azimuthal direction. The two pipes have radii of R_{out1} and R_{out2}. The thickness of the pipes is D. The outer pipe has two defects with angular separation of $\Delta\phi_d$ and opening of L_d and depth of W_d. The inner pipe has one defect with the same size.

TABLE VII
PARAMETER VALUES FOR THE SETUP IN FIG. 9

N_A	$\Delta\phi_a$	R_a	R_{out1}	R_{out2}	D	L_d	W_d	$\Delta\phi_d$
8	30°	47 mm	57.5 mm	79 mm	2 mm	1.5D	0.75D	20°

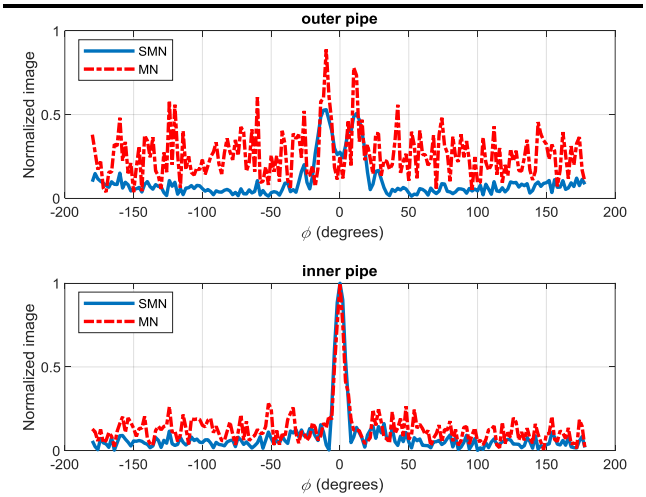

Fig. 10. Reconstructed images in case of N_A = 8 dipole antennas separated at $\Delta\phi_a$ = 30° from each other at a distance of R_a = 47 mm from the center. For this example, the parameters are R_{out1} = 57.5 mm, R_{out2} = 79 mm, D = 2 mm, and SNR = 20 dB.

Gaussian noise with signal-to-noise ratio (SNR) of 20 dB is added to the data. Acquisition of the simulated scattered responses is implemented in a similar way as in the case that the antenna array is placed outside the pipes in section IV.A. Then, holographic imaging is applied on the collected data. The reconstructed images using holographic imaging with MN approach and SMN approach are shown in Fig. 10. When using MN approach, two defects on the outer pipe and one defect on the inner pipe can be reconstructed. However, large artifacts are observed on the reconstructed image of the outer pipe due to the farther distance between the pipe and the antenna array. We can observe significant improvement in the quality of the reconstructed images of the outer and inner pipes when using SMN approach. The reconstruction error when using MN approach, 3.26, is higher than that when using SMN approach,

This article has been accepted for publication in a future issue of this journal, but has not been fully edited. Content may change prior to final publication. Citation information: DOI 10.1109/TIM.2020.2980340, IEEE Transactions on Instrumentation and Measurement

2.18. The resolutions are estimated to be approximately 11 mm and 9.6 mm for the outer and inner pipes, respectively.

C. Cylindrical Scanning and Image Reconstruction with Antenna Array Outside the Pipes

In this section, we study the performance of the system for reconstructing 2D images for each pipe by scanning the pipes over a cylindrical aperture (along both ϕ and z directions).

The values of the parameters are the same as in Table I except the dimensions and locations of the defects. The pipes are with height of 100 mm, relative permittivity ε_r of 2.25, and loss tangent of 0.0004. The antennas scan over a cylindrical aperture with $\Delta\phi = 2°$, $\Delta z = 5$ mm, $z_A = 100$ mm. An X-shape defect is placed at $\phi = 0°$ on the outer pipe while two rectangular defects are placed at $\phi = \pm 90°$ on the inner pipe.

Fig. 11 shows the reconstructed images. The white dashed lines show the true boundaries of the defects. It is observed from Fig. 11(a) that the X-shape defect on the outer pipe can be distinguished when using holographic imaging with MN approach while two rectangular defects on the inner pipe cannot be reconstructed well. After applying holographic imaging with SMN approach, Fig. 11(b) shows that the X-shape defect and two rectangular defects are reconstructed well with drastic quality improvement compared to Fig. 11(a). This demonstrates the capability of the proposed imaging technique in reconstructing the shape of the defects, qualitatively.

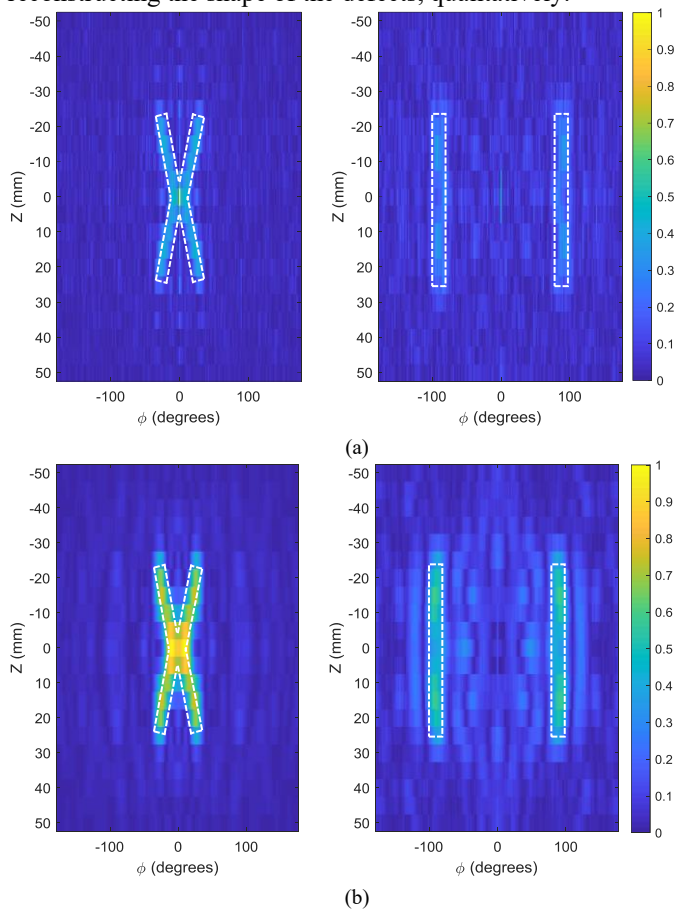

Fig. 11. Reconstructed images when using holographic imaging with: (a) MN approach and (b) SMN approach. The white dashed lines show the true boundaries of the defects.

V. Experimental Results

In this section, in order to validate the proposed imaging technique, we conduct proof-of-concept experiments.

A. Antenna Design and Fabrication

For imaging the pipes, a cavity-backed printed spiral antenna is designed and fabricated. The antenna is designed in FEKO software with the initial target frequency of 6.6 GHz to 8 GHz. This frequency band allows for imaging cylindrical surfaces (pipes) with a separation of approximately 11 mm (quarter wavelength at center frequency) which is suitable, in practice, for standard pipes. Also, the data acquisition systems at this frequency is affordable and cost-effective. This band is within the ultrawide band (UWB) frequency range which has been approved by federal communication commission (FCC) for unlicensed low power applications [36]. Furthermore, when the pipes carry lossy fluids such as mixtures of water with other substances, the penetration of the microwave signals at this band allows for reaching to the pipes farther away from the antennas.

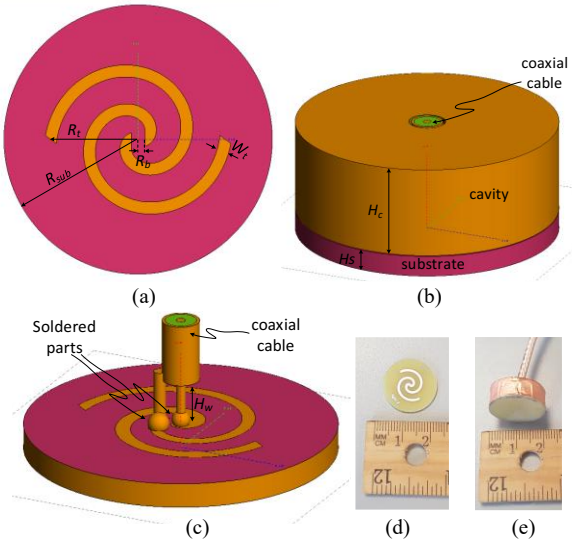

Fig. 12. FEKO simulation model of (a) printed spiral radiators, (b) a cavity placed at the back of the substrate and a coaxial feedline, and (c) connection of the coaxial cable to the printed spiral radiators. Fabricated (d) printed spiral radiators and (e) antenna.

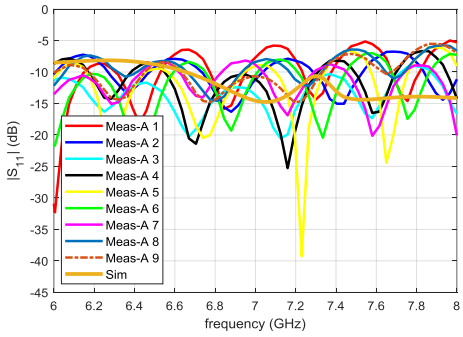

Fig. 13. The measured and simulated $|S_{11}|$ for the antennas.

TABLE VIII
ANTENNA PARAMETERS (ALL UNITS ARE IN MM)

R_{sub}	H_s	R_b	R_t	W_t	H_w	H_c
10	1.6	0.5	6.5	1	3	5

FR4 substrate is used with $\varepsilon_r = 4.8$ and $\tan\delta = 0.017$. To feed the antenna a 50 Ω coaxial cable (inner radius of 0.3 mm and outer radius of 1 mm) is designed and used. In the model, to mimic the practical situation, the shielding of the coaxial cable with a length of H_w is removed right before feeding the printed spiral radiators. A cavity with height of H_c is used to make the antenna directional and eliminate the electromagnetic interferences (EMI). To simplify the fabrication process (soldering), the cavity is placed on the FR4 substrate side for which the spiral radiators are printed. Figs. 12 (a)-(c) show the final design of the antenna and Table VIII shows the optimal parameters. The antenna is fabricated by using the common printed circuit board technology (PCB) for making the spiral radiators and then employing the 3D printing to make the cavity. The material used for 3D printing is Polylactic Acid (PLA). The cavity has a thickness of 1 mm and is covered by adhesive copper sheets. Figs. 12 (d)-(e) show the fabricated antenna. We made 9 of these antennas so that one antenna operates as the transmitter and eight antennas operate as receivers. Fig. 13 shows the comparison between the simulated and measured $|S_{11}|$ for the antenna. Although the antennas are designed to operate within the band of 6.6 GHz to 8 GHz, it is observed that the levels of measured $|S_{11}|$ for most of the antennas are mainly below −10 dB over 6 GHz to 8 GHz band. Thus, we use this frequency band in the following experiments. Besides, the measured responses show oscillations which are associated with some resonance modes not captured well in the simulations. The differences between the measured $|S_{11}|$ for the antenna elements in Fig. 13 are mainly due to the fabrication errors including: small gaps between cavities and antennas when gluing the cavities at the back of the antennas, the slight differences in soldering of cables to the printed spiral radiators, and the slight differences in the length and orientation of the parts of the cables inside the cavities.

B. Image Reconstruction with Data Acquired Outside the Pipes

The antennas are placed inside a holder made by 3D printing and in a configuration similar to the simulation model in Fig. 2, i.e., the angular separation of the antennas is $\Delta\phi_a = 20°$ and the transmitter antenna is placed in the middle (four receiver antennas on each side of that). The antennas are connected to an RF SP8T switch (EV1HMC321ALP4E from Analog Devices operating up to 8 GHz). The RF switch is connected to an Arduino Uno board which can be controlled via MATLAB. We constructed a cylindrical scanning setup with two motors to control the longitudinal and azimuthal movements. The antennas scan double concentric PVC pipes placed inside the antenna holder. Attempts have been made to minimize the gap between the antenna holder and the outer pipe. Fig. 14(a) shows the complete scanning setup when the antenna array is placed outside the pipes. At each sampling step, the complex-valued S parameters are measured via an Anritsu MS46122B vector network analyzer (VNA). The data collection including switching between receiver antennas as well as the control of the scanning system is implemented via MATLAB.

In the experiment, PVC pipes (see Fig. 15) with the outer

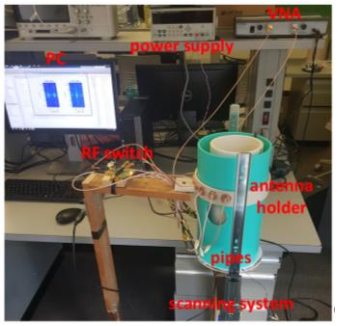

(a)

(b)

Fig. 14. Experimental setup with (a) the antenna array placed outside the pipes and (b) the antenna array placed inside the pipes.

(a) (b) (c)

Fig. 15. (a) Concentric defected pipes with outer and inner diameters of 152.4 mm (6 inch) and 101.6 mm (4 inch), respectively, and (b)-(c) pipes with diameters of 152.4 mm (6 inch) and 101.6 mm (4 inch) with one defect in the middle, respectively.

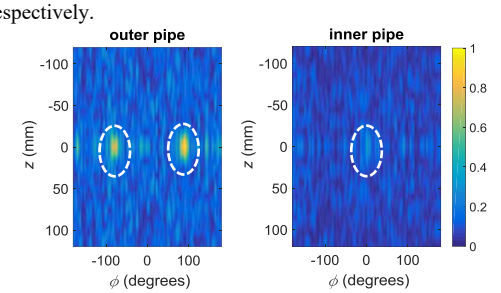

(a)

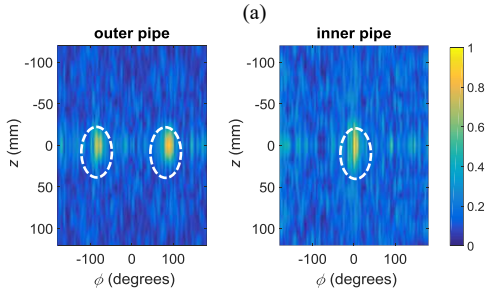

(b)

Fig. 16. Reconstructed images of the inner and outer pipes using experimental data collected by eight receiver antennas outside the pipes when using holographic imaging with: (a) MN approach using 10 frequencies and (b) SMN approach using 10 frequencies.

diameters of 152.4 mm (6 inch) and 101.6 mm (4 inch) are employed. The height of these pipes is 284 mm. The inner pipe has a thickness of 7 mm while the outer one has a thickness of 5 mm. Circular defects with diameters of 55 mm are made on the pipes. We measure PSFs of the outer and inner pipes, separately, using the corresponding pipe with a defect at $(\phi, z) = (0°, 0)$ one at a time. Then, the responses of a test scenario are measured. In the test scenario, two defects are on the outer pipe at $(\phi, z) = (\pm 90°, 0)$ and one defect is on the inner

This article has been accepted for publication in a future issue of this journal, but has not been fully edited. Content may change prior to final publication. Citation information: DOI 10.1109/TIM.2020.2980340, IEEE Transactions on Instrumentation and Measurement

pipe at $(\phi, z) = (0°, 0)$. The PSFs and responses of test scenario are collected over cylindrical aperture with radius of 152.4 mm and height of 240 mm. The number of samples along the ϕ and z directions are 100 and 29, respectively. They are collected at 10 frequencies over the band of 6 GHz to 8 GHz.

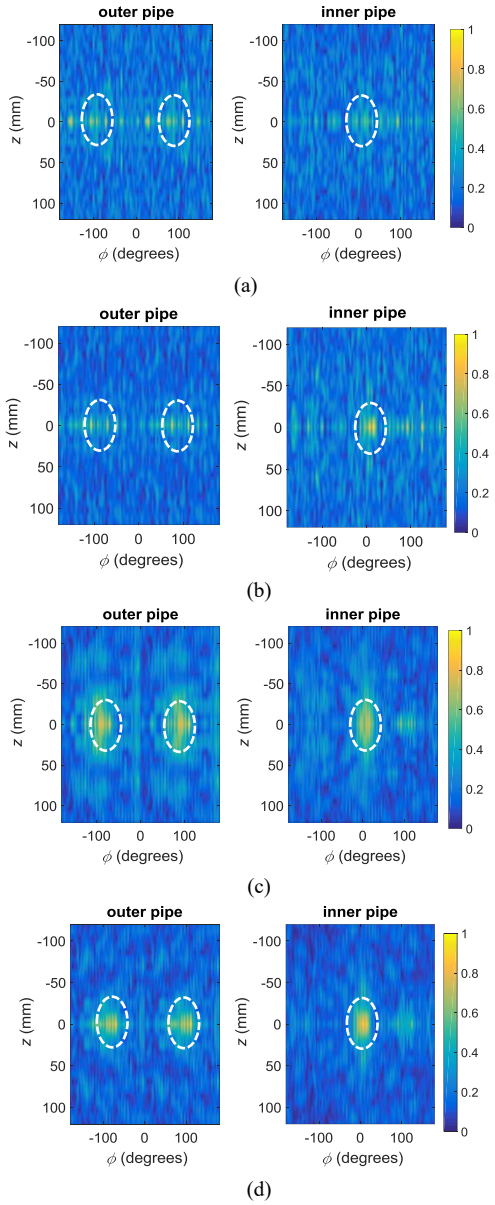

Fig. 17. Reconstructed images of the inner and outer pipes using experimental data collected by eight receiver antennas inside the pipes when using holographic imaging with: (a) MN approach using 10 frequencies, (b) MN approach using 20 frequencies, (c) SMN approach using 10 frequencies, and (d) SMN approach using 20 frequencies.

After applying the holographic imaging with MN approach and with SMN approach to the experimental data collected by eight receiver antennas outside the pipes, reconstructed images of the pipes are obtained. Fig. 16(a) shows the reconstructed images using MN approach. It is observed that two defects on the outer pipe can be reconstructed while the one on the inner pipe cannot be distinguished well. Fig. 16(b) shows the reconstructed images using SMN approach. Compared to Fig. 16(a) it is observed that the defect on the inner pipe can also be reconstructed well.

C. *Image Reconstruction with Data Acquired Inside the Pipes*

In this section, we evaluate the image quality when the antenna array is placed inside the pipes. The antennas are placed inside a holder made by 3D printing and in a configuration similar to the simulation model in Fig. 9 but with the angular separation of the antennas being $\Delta\phi_a = 30°$. Fig. 14(b) shows this configuration.

Similar holographic imaging with MN and SMN approaches are applied to the experimental data collected by eight receiver antennas inside the pipes. Fig. 17(a) shows that the defects on the outer pipe and inner pipe cannot be distinguished clearly when using holographic imaging with MN approach using 10 frequencies over the band of 6 GHz to 8 GHz. Fig. 17 (c) shows the reconstructed images of the pipes when using holographic imaging with SMN approach using 10 frequencies. Compared to Fig. 16(b), the image quality degraded due to the less diverse positions of the antennas leading to acquisition of less information. Besides, due to the use of highly directional antennas, the data collected by some of them (those at larger angular positions from the transmitter) does not contribute much in the image reconstruction. In order to better reconstruct the defects on the pipes, instead of using 10 frequencies within the band of 6 GHz to 8 GHz, 20 frequencies within the same band are used to reconstruct images. Fig. 17(b) shows the defects on the outer pipe cannot be detected well but the one on the inner pipe can be distinguished with MN approach using 20 frequencies. After applying the holographic imaging with SMN approach, defects on the outer pipe and inner pipe can be reconstructed well as shown in Fig. 17(d). However, the quality of reconstructed images is still not as good as the one shown in Fig. 16(b) (when the antennas are outside the pipes).

VI. Discussion and Conclusion

In this paper, we proposed an NDT technique based on microwave holographic imaging augmented by an SMN approach for solving the systems of equations. In general, this showed remarkable improvement in the quality of the reconstructed images compared to the conventionally used MN approach although in few cases (e.g., see Figs. 4 and 8) the resolution of the images along the azimuthal direction degrades. FEKO simulations are performed to study the effects of standoff distance, number of receiver antennas, angular separation between the antennas, inner pipe radius (gap between the two pipes), and pipe thickness when the array of antennas is scanning outside the pipes. To summarize, according to our study, smaller standoff distance, more receiver antennas, and sufficiently large angular separation between the receiver antennas improve the image reconstruction quality. The optimal values of these parameters depend on the dimensions of the PUTs. Also, please note that, the parameter values of the *reference setup* are not necessarily optimal. However, the parametric study in Tables II-VI allows one to understand the effects of the main parameters of the setup. We also demonstrated the possibility of reconstructing images

when the array of antennas is scanning inside the pipes. Besides, an experimental setup including a designed cavity-backed printed spiral antenna is constructed to acquire data in two different scenarios including antennas outside the pipes and inside the pipes.

According to our study: (1) the defects on two concentric pipes can be reconstructed, (2) the quality of the reconstructed images using holographic imaging with SMN approach is significantly higher than the one using MN approach, (3) the quality of the reconstructed images is higher when the array of antennas is scanning outside the pipes (deduced from comparing Figs. 16 and 17 when using 10 frequencies) due to the fact that the antennas are in more diverse positions leading to collecting more information, and (4) having the antennas outside the pipes allows for using more directional antennas to focus the microwave power toward the pipes and to mitigates the EMI (effect of any materials outside the pipes, etc.), significantly, and (5) the uncertainty in the gap between the antennas and the pipes significantly affects the quality of the reconstructed images. To minimize that in the experimental setup, the antenna holders were designed such that the antennas maintained direct contact with the pipes during the scan.

Some of the limitations for the proposed imaging technique, include: (1) the media inside and around the pipes should be homogeneous, (2) the imaging system should be shielded to avoid interferences and back-scattering from objects outside the pipes, (3) as a holographic imaging technique, it provides qualitative images (it recovers the shape of the defects but not the thickness of the pipes in the defected region), and (4) the effects of fluids flowing inside the pipes have not been considered (assuming the pipes are tested while they are empty). Their loss, dispersion, and high contrast with respect to the air affect the performance of the system although the resolution may be improved due to their higher permittivity. Besides, in this scenario, PSFs should be collected with the presence of fluids.

In practice, the scattered responses can be obtained by subtracting the background responses, obtained by one of the following methods: (1) the responses of similar pipes recorded without the presence of the defects, (2) the average of measured response along ϕ and z, recorded with the presence of the defects, assuming that the defects are small, or (3) the scattered responses with the presence of the defects but at positions far away from them to ensure negligible contribution of the defect's response. We studied the above-mentioned methods and for the simulated and experimental examples, in this work, they worked equally well. Besides, the PSFs need to be measured *a prior* along ϕ and z. We can establish a database for PSFs of the pipes of specific materials and dimensions by measuring such configurations then use the collected information for imaging of the corresponding PUTs. Obtaining PSF information via measurements significantly reduces the modeling errors, errors due to the uncertainties of the material properties used in analytical expressions of the incident field and Green's function, and errors due to the size of the antennas.

For thin pipes (studied in this work), there is no noticeable difference between the qualities of the images when the CDs are placed on the outer or inner surfaces of the pipes. However, for thicker pipes, we expect that the placement of the CD would affect the quality of the reconstructed images depending on the defects being on the inner or outer surfaces of the pipes. In practice, the CD is the smallest defect that the system can measure which, in turn, depends on the dynamic range of the data acquisition setup. This indicates that CD can be different for each pipe and at each frequency range. Parameters that influence the dynamic range of the system include: noise floor of the data acquisition system, mechanical ripples, and other uncertainties in the measurement setup. The chosen CDs based on the above-mentioned factors are the building blocks for any larger arbitrary defect to be reconstructed.

To expedite the data acquisition process and improve the robustness of the system, an electronically switched antenna array similar to the security screening systems in the airports [37], [38] can be implemented.

By employing the proposed NDT system, non-metallic concentric pipes can be inspected in a reliable and robust manner which would promote their use in various industrial sectors, for instance, in oil and gas field.

ACKNOWLEDGMENT

This project has been supported by US national science foundation (NSF), award No. 1920098, and New York Institute of Technology's (NYIT) Institutional Support for Research and Creativity (ISRC) Grants.

REFERENCES

[1] J. Blitz and G. Simpson, *Ultrasonic Methods of Non-destructive Testing*. Chapman & Hall London, 1996.

[2] W. M. Alobaidi, E. A. Alkuam, H. M. Al-Rizzo, and E. Sandgren, "Applications of ultrasonic techniques in oil and gas pipeline industries: a review," *American J. of Operations Research*, vol. 5, pp. 4, Jul. 2015.

[3] L. Tong, A. P. Mouritz, and M. K. Bannister. *3D Fiber Reinforced Polymer Composites*. 1st ed. The Boulevard, Langford Lane, Kidlington, Oxford, UK: Elsevier Science Ltd., 2002. ISBN: 0080439381.

[4] K. Murphy and D. Lowe, "Evaluation of a novel microwave based NDT inspection method for polyethylene joints," in *Proc. ASME Pressure Vessels Piping Conf.*, Baltimore, MD, USA, 2011, pp. 321–327.

[5] X. W. Zhu, J. P. Pan, and L. J. Tan, "Microwave scan inspection of HDPE piping thermal fusion welds for lack of fusion defect," *Appl. Mech. Mater.*, vols. 333–335, pp. 1523–1528, Jul. 2013.

[6] R. Pincu, "Digital radiography and its advantages in field NDT inspections today," *17th World Conf. on Nondestructive Testing*, Shanghai, China Oct. 2008.

[7] R. Zoughi, *Microwave Non-Destructive Testing and Evaluation*. Kluwer Academic Publishers, 2000.

[8] S. Kharkovsky and R. Zoughi, "Microwave and millimeter wave nondestructive testing and evaluation - Overview and recent advances," *IEEE Instr. and Meas. Mag.*, vol. 10, no. 2, pp. 26–38, April 2007.

[9] R. J. Stakenborghs, "Microwave inspection method and its application to FRP," *MTI AmeriTAC 110 Conf. (MTI AmeriTAC)*, 2013.

[10] R. Stakenborghs, "Microwave based NDE inspection of HDPE pipe welds," *17th Int. Conf. on Nuclear Engineering ICONE17*, 2009.

[11] K. Schmidt, T. Aljundi, G. A. Subaii, and J. Little, "Microwave interference scanning inspection of nonmetallic pipes," *5th Middle East Nondestructive Testing Conf. & Exhibition*, Manama, Bahrain 2009.

[12] D. M. Tripathi, S. Gunasekaran, S. S. Murugan, and N. A. Enezi, "NDT by microwave test method for non metallic component," *Indian National Seminar & Exhibition on Non-Destructive Evaluation NDE*, 2016.

[13] T. D. Carrigan, B. E. Forrest, H. N. Andem, K. Gui, L. Johnson, J. E. Hibbert, B. Lennox, and R. Sloan, "Nondestructive testing of nonmetallic pipelines using microwave reflectometry on an in-line inspection robot," *IEEE Trans. Inst. Meas.*, vol. 68, no. 2, pp. 586–594, Feb. 2019.

[14] M. T. Ghasr, K. Ying, and R. Zoughi, "3D millimeter wave imaging of vertical cracks and its application for the inspection of HDPE pipes," *AIP Conf. Proc.*, vol. 1581, no. 1, pp. 1531–1536, 2014.
[15] Laviada, J., B. Wu, M.T. Ghasr, and Reza Zoughi, "Nondestructive evaluation of microwave-penetrable pipes by synthetic aperture imaging enhanced by full-wave field propagation model," *IEEE Trans. on Instrum. and Meas.*, vol. 68, no. 4, pp. 1112-1119, Apr. 2019.
[16] B. Wu, Y. Gao, J. Laviada, M. T. Ghasr and R. Zoughi, "Time-reversal SAR imaging for nondestructive testing of circular and cylindrical multi-layered dielectric structures," *in IEEE Trans. on Instrum. and Meas*.
[17] M. D. Buhari, G. Y. Tian and R. Tiwari, "Microwave-based SAR technique for pipeline inspection using autofocus Range-Doppler algorithm," in *IEEE Sensors Journal*, vol. 19, no. 5, pp. 1777-1787, 1 March1, 2019.
[18] R. K. Amineh, N. K. Nikolova, and M. Ravan, *Real-Time Three-Dimensional Imaging of Dielectric Bodies Using Microwave/Millimeter Wave Holography*. Wiley & IEEE Press, ISBN: 978-1-119-53886-8, 2019.
[19] M. Ravan, R. K. Amineh, and N. K. Nikolova, "Two-dimensional near-field microwave holography," *Inverse Problems*, vol. 26, 2010, 055011.
[20] R. K. Amineh, M. Ravan, A. Khalatpour, and N. K. Nikolova, "Three-dimensional near-field microwave holography using reflected and transmitted signals," *IEEE Trans. on Antennas Propag.*, vol. 59, no. 12, pp. 4777–4789, Dec. 2011.
[21] R. K. Amineh, A. Khalatpour, H. Xu, Y. Baskharoun, and N. K. Nikolova, "Three-dimensional near-field microwave holography for tissue imaging," *Int. J. of Biomed. Imag.*, vol. 2012, p. 291494, 2012.
[22] R. K. Amineh, M. Ravan, J. McCombe, and N. K. Nikolova, "Three-dimensional microwave holographic imaging employing forward-scattered waves only," *Int. J. of Antennas Propag.*, vol. 2013, Article ID 897287, 2013.
[23] R. K. Amineh, J. McCombe, A. Khalatpour, and N. K. Nikolova, "Microwave holography using point-spread functions measured with calibration objects," *IEEE Trans. on Inst. and Meas.*, vol. 64, no. 2, pp. 403−417, 2015.
[24] L. E. S. Martin, A. E. Fouda, R. K. Amineh, I. Capoglu, B. Donderici, S. S. Roy, F. Hill, "New high-definition frequency tool for tubing and multiple casing corrosion detection," *SPE Abu Dhabi Int. Petroleum Exhibition & Conference*, 2017.
[25] Y. Renardy, D. D. Joseph, "Couette flow of two fluids between concentric pipes," *J. of Fluid Mechanics*, vol. 150, pp. 381–394, Jan. 1985.
[26] H. Wu and R. K. Amineh, "Near-field holographic microwave imaging using data collected over cylindrical apertures," *18th Int. Symp. on Antenna Tech. and Applied Electromag. (ANTEM)*, 2018.
[27] R. K. Amineh, M. Ravan, H. Wu, and A. Kasturi, "Three-dimensional holographic imaging using data collected over cylindrical apertures," *Microw. Opt. Technol. Lett.*, 2018. DOI: 10.1002/mop.31694.
[28] H. Wu and R. K. Amineh, "A low-cost and compact three-dimensional microwave holographic imaging system," *Electronics*, vol. 8, no. 9, 2019.
[29] R. K. Amineh, M. Ravan, R. Sharma, and S. Baua, "Three-dimensional holographic imaging using single frequency microwave data," *Int. J. of Antennas and Propag.*, vol. 2018, Article ID 6542518, 14 pages, 2018.
[30] A. V. Oppenheim, R. W. Schafer, and J. R. Buck. *Discrete-Time Signal Processing.* 2nd ed. Upper Saddle River, NJ: Prentice Hall, 1999. ISBN: 0137549202.
[31] R. D. Pascual-Marqui, "Standardized low resolution brain electromagnetic tomography (sLORETA): technical details," *Methods Find. Exp. Clin. Pharmacol*., vol. 24, suppl D:5-12, pp. 1–16, 2002.
[32] D. Garcia, "Robust smoothing of gridded data in one and higher dimensions with missing values," *Comput. Stat. Data. Anal.*, vol. 54, no. 4, pp. 1167–1178, Apr. 2010.
[33] A. M. Dale, A. K. Liu, B. R. Fischl, R. L. Buckner, J. W. Belliveau, J. D. Lewine, and E. Halgren, "Dynamic statistical parametric mapping: combining fMRI and MEG for highresolution imaging of cortical activity," *Neuron*, vol. 26, pp. 55–67, 2000.
[34] R. K. Amineh and G. V. Eleftheriades, "2D and 3D sub-diffraction source imaging with a superoscillatory filter," *Optics Express*, vol. 21, no. 7, pp. 8142−8157, 2013.
[35] J. W. Goodman, *Introduction to Fourier Optics*, McGraw-Hill, 1996.
[36] Federal Communication Commission (FCC) report and order, Feb. 14, 2002, http://hraunfoss.fcc.gov/edocs_public/attachmatch/ FCC-02-48A1.pdf
[37] D. M. Sheen, D. L. McMakin, and T. E. Hall, "Three-dimensional millimeter-wave imaging for concealed weapon detection," *IEEE Transactions on Microwave Theory and Techniques*, vol. 49, no. 9, pp. 1581–1592, Sep. 2001.
[38] D. M. Sheen, D. L. McMakin, and T. E. Hall, "Near-field three-dimensional radar imaging techniques and applications," *Applied Optics*, vol. 49, no. 19, pp. E83–E93, June 2010.

Hailun Wu is currently a Research Assistant in the Applied Electromagnetics Research Lab at New York Institute of Technology (New York Tech). She received B.Eng. degree in Opto-electronics Engineering from Shenzhen University in 2017. She received her M.Sc. degree with distinction in Electrical and Computer Engineering from New York Tech in 2019. She has been with the Applied Electromagnetics Research Lab at New York Tech as a research assistant since 2017. Her research interests include microwave holographic imaging techniques, non-destructive testing, image reconstruction, microwave imaging systems, and RF& Microwave circuit design. She is a member of IEEE.

Maryam Ravan (M'10—SM'12) received her Ph.D. degree from Amirkabir University of Technology, Tehran, Iran. She was a postdoctoral fellow with the Departments of Electrical and Computer Engineering at University of Toronto, McMaster University, and Ryerson University, Ontario, Canada, from May 2007 to April 2013, where she was involved in solving forward modeling and inverse problems and the related signal/image processing techniques for biomedical, radar systems, microwave imaging, and non-destructive testing (NDT) applications. She was also a lecturer in the School of Computational Engineering & Science, McMaster University, Canada, from 2009 to 2012. From May 2013 to August 2017, she was a Senior Research Scientist in the Department of Research and Development at LivaNova PLC, where her work focused on developing quantitative biomarkers and machine learning algorithms for investigating the efficacy of closed-loop Vagus nerve stimulation (VNS) therapy for epilepsy. She is currently an Assistant Professor in the Department of Electrical and Computer Engineering, New York Institute of Technology. Her research interests include signal and image processing, beamforming, machine learning, microwave holography, MIMO radar systems and space time adaptive processing, and nondestructive testing. Dr. Ravan has authored/coauthored over 70 journal and conference papers, a book chapter, and a book. Her research has been supported by US National Science Foundation (NSF), DND/NSERC Research Partnership Grant with Defense Research and Development Canada (DRDC) and Raytheon Canada Ltd, MITACS Internship with St. Joseph's Hospital in Hamilton, Canada, and NSERC Engage Grant with Raytheon Canada Ltd.

Raveena Sharma is currently an RF Development Engineer at Electro-metrics Corporation. Prior to this, she was an Electrical Testing and LabView Engineer at HeliTrak Inc. She received her M.Sc. with distinction in Electrical and Computer Engineering from New York Institute of Technology (New York Tech). She was the recipient of the New York Tech Electrical and Computer Engineering Graduate Faculty Award, 2019. During her Master's program, she was a research assistant working on microwave imaging using holographic techniques as well as efficient deployment of UAV in disaster areas. Her research interests include applied electromagnetics, microwave imaging, and non-destructive testing. She is a student member of IEEE.

Jay Patel received the B.S. degree in Electronics and Communication from Charotar University of Science and Technology (CHARUSAT), Changa, Gujarat, India, in 2018. He is currently pursuing the M.Sc. in Electrical and Computer Engineering at New York Institute of Technology, USA. He is currently working as a Research Assistant in the Applied Electromagnetics Research Lab, New York Institute of Technology where he is involved in designing Surface Integrated Waveguide (SIW) antennas and Cavity backed Spiral antennas.

Reza K. Amineh (S'08–M'11–SM'13) is currently an Assistant Professor in the Department of Electrical and Computer Engineering, New York Institute of Technology. Prior to that, he was a Principal Scientist in the Department of Sensor Physics at Halliburton Co. He received his Ph.D. degree in electrical engineering from McMaster University, Canada, in 2010. He was a post-doctoral fellow at University of Toronto and McMaster University, from 2012 to 2013 and from 2010 to 2012, respectively. He was a Ph.D. intern with the Advanced Technology Group, BlackBerry, in 2009. He has authored/co-authored over 75 journal and conference papers, two book chapters, and a book titled "Real-Time Three-Dimensional Imaging of Dielectric Bodies Using Microwave/Millimeter Wave Holography" published by Wiley & IEEE Press. He contributed in more than 40 patent disclosures in applied electromagnetics while working at Halliburton Co and received several industrial awards. His research interests include applied electromagnetics with applications in imaging and sensing. Amineh was a recipient of the Banting Post-Doctoral Fellowship from the Government of Canada in 2012 and the Ontario Ministry of Research and Innovation (OMRI) Post-Doctoral Fellowship in 2010. During his Ph.D. program, he was awarded the McMaster Internal Prestige Scholarship Clifton W. Sherman for two consecutive years. He has co-authored a paper selected as a finalist in the student paper competition at IEEE Wireless and Microwave Technology Conference in 2019, an Honorable Mention Paper presented at the IEEE Symposium on Antennas and Propagation in 2008, and a paper selected among the journal of Inverse Problems' "Highlights Collection of 2010". Amineh is a senior member of IEEE.